GEOPHYSICS, VOL. 89, NO. 1 (JANUARY-FEBRUARY 2024); P. T1–T11, 18 FIGS.
10.1190/GEO2023-0176.1

Check for updates

Downloaded 01/12/24 to 138.67.12.184. Redistribution subject to SEG license or copyright; see Terms of Use at http://library.seg.org/page/policies/terms
DOI:10.1190/geo2023-0176.1

Modeling the seismic wavefield of moving marine vibrator source

Khalid Almuteri[1], Jeffrey Shragge[1], and Paul Sava[1]

ABSTRACT

Marine vibrators are an emerging alternative to conventional air guns in ocean-bottom acquisition due to their ability to generate low-frequency waves and limited adverse impact on marine wildlife. However, using marine vibrators introduces challenges not found in conventional air-gun-based acquisition where receivers are placed on the ocean bottom, including handling the phenomena associated with the Doppler effect and time-dependent source-receiver offsets due to the source motion. Standard seismic data processing solutions assume stationary sources and receivers for the duration of any seismic experiment (e.g., a shot); however, accurately accounting for source motion effects in processing is critical for optimal subsurface imaging. To address these challenges, we develop a finite-difference approach for modeling the full acoustic wavefield in a generalized coordinate system that tracks a moving source. Synthetic examples demonstrate that this technique accurately and stably models high-velocity moving sources and accurately accounts for the wavefield distortion predicted by the Doppler effect. This approach is not limited to modeling wavefield propagation for a moving source and can be used to develop advanced imaging and inversion techniques (e.g., reverse time migration and full waveform inversion) for data acquired using marine vibrators. In addition, the developed approach is not only limited to modeling mobile sources but also can model conventional towed-streamer data.

INTRODUCTION

Concerns over conventional seismic air guns make a transition to less environmentally adverse marine vibrators desirable. Although marine vibrators have been around since the 1960s (Smith and Jenkerson, 1998), the lack of low frequencies and the perceived unreliability of marine vibrators have historically prevented further development and interest by the exploration industry in the technology (Teyssandier and Sallas, 2019). However, recent technological advancements renewed the interest in marine vibrators not only for environmental reasons but also for their geophysics-related merits. From a seismic exploration perspective, marine vibrators can provide richer low-frequency content than air guns (Dellinger et al., 2016; Guitton et al., 2021) and enable versatile control over the source signature (Laws et al., 2019). Unlike air guns, for which phase can only be modified through time delays, the phase in marine vibrators can be independently specified for each frequency. The precise control over phase in marine vibrators allows for the use of advanced acquisition techniques such as phase sequencing, creating source-side wavefield gradients, and simultaneous acquisition, as discussed in the following:

- Phase sequencing in cascaded sweep acquisition helps attenuate residual source noise, allowing for denser shot acquisition in the inline direction (Laws et al., 2019). In air-gun-based acquisition, a sufficient time period must pass between acquiring two consecutive shots for the shot-generated noise from a shot to be at an acceptable level when acquiring the subsequent shot (Landrø, 2008). This trade-off between source-time interval and the level of residual source noise results in suboptimal and sparser shot acquisition than desirable. Varying the source phase from one source point to the next can resolve the sparsity of source points in marine data inline. In practice, such changes are difficult to execute using seismic air guns but easily attainable using marine vibrator sources.
- Crossline sampling in marine acquisition often is sparse, resulting in aliased wavefields. One method for reconstructing the nonaliased seismic wavefield uses the multichannel sampling theorem, which extends Shannon's sampling theorem by incorporating the spatial derivative of the seismic wavefield in the reconstruction process (Robertsson et al., 2008; Vassallo et al., 2010; Pawelec et al., 2022). This method reduces the necessary spatial sampling and enables the recov-

Manuscript received by the Editor 11 March 2023; revised manuscript received 8 August 2023; published ahead of production 29 September 2023; published online 11 December 2023.
[1]Colorado School of Mines, Center for Wave Phenomena, Department of Geophysics, Golden, Colorado, USA. E-mail: kalmuteri@mines.edu (corresponding author); jshragge@mines.edu; psava@mines.edu.
© 2024 Society of Exploration Geophysicists. All rights reserved.

Downloaded 01/12/24 to 138.67.12.184. Redistribution subject to SEG license or copyright; see Terms of Use at http://library.seg.org/page/policies/terms
DOI:10.1190/geo2023-0176.1

ery of nonaliased data from aliased input, allowing for data to be acquired twice as coarsely as when not using the spatial derivative data along the crossline direction (Laws et al., 2019). Thus, acquiring the source-side spatial gradient of the pressure wavefield facilitated by marine vibrator sources can effectively address the issue of spatial aliasing in the crossline direction. Such data can be acquired using two marine vibrators, placed with some offset along the crossline direction, sweeping with opposite polarities. The corresponding air gun acquisition would require sailing each inline twice or acquiring secondary data in the vicinity of primary source points, using an approach similar to over/under sources (e.g., Egan et al., 2007) to estimate the source-side wavefield gradient in the crossline direction.

- Another advantage of using marine vibrators is acquiring seismic data in a shorter time compared with air-gun-based acquisition when using multiple phase-encoded sources simultaneously. Although simultaneous acquisition is achievable using seismic air guns (e.g., Mueller et al., 2015; Robertsson et al., 2016; Amundsen et al., 2018), the limited phase control in seismic air guns limits the full potential of simultaneous acquisition (Halliday and Moore, 2018; Laws et al., 2019). Laws et al. (2019) numerically demonstrate that using the aforementioned techniques can reduce acquisition time by one-third compared with conventional air-gun acquisition without compromising the quality of the seismic images.

Processing and imaging challenges emerge due to the source motion and long duration of the marine vibrator sweep, including the Doppler effect and time-dependent source-receiver offsets in ocean-bottom acquisition. Even though marine vibrators move at a much slower velocity than the wave propagation speed, source motion introduces a noticeable offset- and time-dependent frequency shift to the data (Dragoset, 1988; Schultz et al., 1989; Hampson and Jakubowicz, 1995). Also, phase distortion occurs in the seismic signal, which is proportional to the source velocity and time slope of seismic events because of the source motion.

Current seismic data processing and imaging in marine acquisition assume stationary geometry for the duration of a seismic experiment. Appropriate processing and imaging of data acquired using moving sources requires accurate modeling of the associated effects. Numerical wave equation solutions are necessary for understanding wave propagation under realistic acquisition conditions (e.g., dynamic sea surfaces and/or moving sources) and form the basis of many geophysical applications such as imaging and inversion. Accurate modeling of seismic wavefields is key in advanced seismic imaging and inversion techniques, such as reverse time migration (RTM) (e.g., Almuteri et al., 2022) and full waveform inversion (FWI) (e.g., Kurzmann et al., 2013; Zhou et al., 2018; Zhang et al., 2023). Various methods are proposed in the literature to model marine vibrator data. Dellinger and Díaz (2020) present a sweep segmentation approach to model mobile sources that splits the source function into different segments that can be injected at fixed source positions along the source path. The advantage of this approach is its simplicity and ease of implementation. However, it may require applying a correction filter to the modeled data (Duquet et al., 2021) because it assumes the source jumps to discrete locations along the source path instead of being continuously in motion. JafarGandomi and Grion (2021) propose a method of modeling marine vibrator data by interpolating unaliased impulsive sources data to desired source locations and convolving with segments of the vibrator sweep. This method is similar to the former approach because it also uses a source-segmentation technique. However, this method requires densely sampled sources and data interpolation, which can be computationally expensive for irregularly sampled sources. Cartesian-based modeling methods are susceptible to numerical instabilities and modeling inaccuracies when introducing irregular or dynamic computational geometries such as time-varying sea surfaces (Konuk and Shragge, 2020). Further challenges arise when implementing free-surface boundary conditions for such irregular geometries in a Cartesian coordinate system.

This paper presents a finite-difference (FD) approach to model the full acoustic wavefield triggered by a mobile source in a generalized coordinate system that effectively embeds source motion into the coefficients of the governing tensorial acoustic wave equation (AWE). Shragge (2014) and Shragge and Tapley (2017) present a time-invariant tensorial representation of the AWE in a generalized coordinate system. This approach facilitates coordinate transformation to map the irregular physical domain to a regular computational domain, enabling FD modeling. Konuk and Shragge (2020) extend this technique to address the challenge of dynamic sea surfaces by specifying a time-variant 4D coordinate transformation. This extension leads to a time-varying mesh grid in physical Cartesian coordinates but a stationary mesh grid in a generalized computational coordinate system.

Here, we present a solution to the AWE for a time-varying mesh without the need for repeated velocity model interpolation, eliminating the added computational complexity and accuracy issues associated with this operation. In this framework, the time-varying physical Cartesian domain horizontally shears conformally with the source motion. However, the computational domain is fixed in time, with time- and space-dependent partial differential operator coefficients. The developed approach is not limited to modeling moving sources with ocean-bottom receivers but also is applicable to conventional towed-streamer scenarios. In addition, we investigate source motion effects on seismic data, including ghost reflections, acquired under a quiescent sea surface condition.

THEORY

Tensorial acoustic wave equation

The 4D tensorial AWE in a generalized coordinate system defined by the variables $\boldsymbol{\xi} = [\xi^0, \xi^1, \xi^2, \xi^3]$ is (Konuk and Shragge, 2020)

$$\square_\xi P_\xi = F_\xi, \tag{1}$$

where $\square_\xi$ is the generalized d'Alembert operator, P_ξ is the pressure field, and F_ξ is the source function. The ξ^0 coordinate is the time-like component (time axis scaled by the acoustic velocity) and ξ^1, ξ^2, and ξ^3 are the space-like components. The generalized d'Alembert operator is

$$\square_\xi = \frac{-1}{\sqrt{|\mathbf{g}|}} \frac{\partial}{\partial \xi^\mu} \left(\sqrt{|\mathbf{g}|} g^{\mu\nu} \frac{\partial}{\partial \xi^\nu} \right), \quad \mu, \nu = 0, \ldots, 3, \tag{2}$$

where $[g^{\mu\nu}]$ is a symmetric rank-two contravariant metric tensor, $|\mathbf{g}|$ is the determinant of the covariant metric tensor $[g_{\mu\nu}]$, and

Downloaded 01/12/24 to 138.67.12.184. Redistribution subject to SEG license or copyright; see Terms of Use at http://library.seg.org/page/policies/terms
DOI:10.1190/geo2023-0176.1

$[g^{\mu\nu}] = [g_{\mu\nu}]^{-1}$. Here, we use superscript indices for components with a contravariant representation and subscript indices for components with a covariant representation. The covariant metric tensor relates the generalized coordinate geometry to an equivalent Cartesian coordinate system representation with elements given by

$$g_{\mu\nu} = \frac{\partial x^i}{\partial \xi^\mu}\frac{\partial x^i}{\partial \xi^\nu} \quad \text{for } i,\mu,\nu = 0,\ldots,3, \tag{3}$$

where repeated indices imply summation. The columns of the contravariant and covariant metric tensors form dual bases (i.e., the dot product $\langle \mathbf{g}_i, \mathbf{g}^j \rangle = \delta_{ij}$). In Cartesian coordinates with variables $\mathbf{x} = [x^0, x^1, x^2, x^3] = [ct, x, y, z]$, the d'Alembert operator (equation 2) reduces to

$$\Box = \frac{-1}{c^2}\frac{\partial^2}{\partial t^2} + \nabla^2, \tag{4}$$

where $c = c(\mathbf{x})$ is the Cartesian medium velocity and ∇^2 is the 3D Cartesian Laplacian operator.

To simulate wavefields triggered by a moving source, we set the generalized AWE in arbitrary coordinates and then choose a coordinate transformation that maps a horizontally deformed physical domain to a regular computational domain. To simplify the 4D coordinate transformation, we make a set of plausible assumptions: (1) no stretching of the time coordinate occurs, i.e., $x^0 = \xi^0$ (or $t = \tau$); (2) the horizontal source movement is along the ξ^1-axis only, leaving the ξ^2-axis unchanged (i.e., $x^2 = \xi^2$); (3) the source moves at a fixed depth level (i.e., there is no vertical motion and thus $x^3 = \xi^3$); (4) the source moves at a constant velocity (i.e., $(\partial v/\partial \xi^0) = 0$); and (5) the source moves in a homogeneous fluid medium. The first four assumptions allow us to express the horizontal mesh deformation $x^1 = T(\xi^0, \xi^1, \xi^2, \xi^3)$, where T is any arbitrary horizontal deformation function that depends on all variables $(\xi^0, \xi^1, \xi^2, \xi^3)$. Recognizing that $\xi^0 \equiv c\tau$ and $(\partial/\partial\xi^0) = (1/c)(\partial/\partial\tau)$, the generalized d'Alembert operator (equation 2) for an arbitrarily deformed mesh along the ξ^1-axis reduces to the second-order AWE:

$$\underbrace{\frac{1}{T_1}\frac{\partial}{\partial\tau}\left(\frac{T_1}{c^2}\frac{\partial P_\xi}{\partial\tau}\right)}_{\text{Newtonian acceleration}} = \underbrace{\frac{1}{T_1}\left[\frac{\partial}{\partial\xi^1}\left(\frac{T_0}{c}\frac{\partial P_\xi}{\partial\tau}\right) + \frac{\partial}{\partial\tau}\left(\frac{T_0}{c}\frac{\partial P_\xi}{\partial\xi^1}\right)\right]}_{\text{Fluid advection}} + \underbrace{\frac{1}{T_1}\frac{\partial}{\partial\xi^i}\left(T_1 g^{ij}\frac{\partial P_\xi}{\partial\xi^j}\right)}_{\text{Restoring force}} + F_\xi, \tag{5}$$

where $T_k = (\partial T/\partial\xi^k)$ and $i,j = 1,2,3$ are the spatial indices. The assumptions stated previously allow us to express the relationship between the $\boldsymbol{\xi}$- and $\mathbf{x}$-coordinate systems as

$$\begin{bmatrix} x^0 \\ x^1 \\ x^2 \\ x^3 \end{bmatrix} = \begin{bmatrix} \xi^0 \\ T(\xi^0,\xi^1,\xi^2,\xi^3) \\ \xi^2 \\ \xi^3 \end{bmatrix} = \begin{bmatrix} \xi^0 \\ \xi^1 + v\tau e^{\gamma(s_z - \xi^3)} \\ \xi^2 \\ \xi^3 \end{bmatrix}, \tag{6}$$

where v is the constant source velocity, γ is a user-defined decay factor that controls the amount of horizontal deformation as a function of depth, and s_z is the source depth. We confine the time-varying mesh deformation to the homogeneous water layer by introducing a depth-dependent horizontal deformation. This coordinate transformation enables the modeling of a moving source without the need for velocity model interpolation at each time step. Furthermore, it allows one to compute the wavefield at and below the receivers level in ocean-bottom acquisition without the need to interpolate the wavefield to Cartesian coordinates. Figure 1a and 1b shows a deformed physical domain in Cartesian coordinates and the fixed computational domain in a generalized coordinate system, respectively. At the initial time, the computational and physical domains are identical (i.e., $x^1 = \xi^1$). Extending this approach to include a moving source with a time-dependent velocity, i.e., $v \to v(\xi^0)$, is straightforward.

The contravariant metric tensor associated with the depth-dependent horizontally shearing coordinate transformation (equation 6) is

$$[g^{\mu\nu}] = \frac{1}{c^2}\begin{bmatrix} -1 & v\alpha & 0 & 0 \\ v\alpha & v^2\alpha^2[\beta^2 - 1] + c^2 & 0 & c\beta v\alpha \\ 0 & 0 & c^2 & 0 \\ 0 & c\beta v\alpha & 0 & c^2 \end{bmatrix}, \tag{7}$$

where $\alpha = e^{\gamma(s_z - \xi^3)}$ and $\beta = c\gamma\tau$. Thus, equation 5 reduces to

$$\begin{aligned} \frac{1}{c^2}\frac{\partial}{\partial\tau}\left(\frac{\partial P_\xi}{\partial\tau}\right) &= \frac{2v\alpha}{c^2}\frac{\partial}{\partial\xi^1}\left(\frac{\partial P_\xi}{\partial\tau}\right) \\ &+ \left[\gamma^2\tau^2 v^2\alpha^2 - \frac{v^2\alpha^2}{c^2}\right]\frac{\partial}{\partial\xi^1}\left(\frac{\partial P_\xi}{\partial\xi^1}\right) \\ &- \gamma^2\tau v\alpha\frac{\partial P_\xi}{\partial\xi^1} + 2\gamma\tau v\alpha\frac{\partial}{\partial\xi^1}\left(\frac{\partial P_\xi}{\partial\xi^3}\right) + \nabla^2_\xi P_\xi + F_\xi, \end{aligned} \tag{8}$$

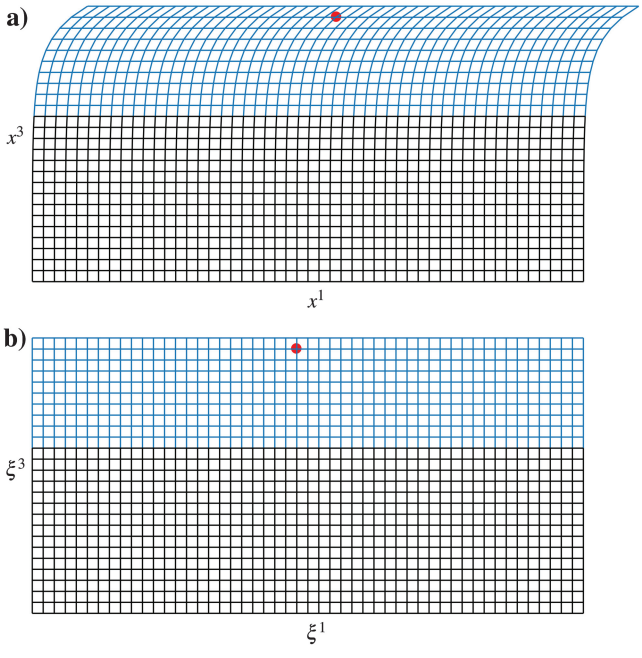

Figure 1. Graphical representation of (a) physical and (b) computational domains. The red dot indicates the source location. The blue mesh represents a homogeneous region, whereas the black mesh represents a variable velocity region.

Downloaded 01/12/24 to 138.67.12.184. Redistribution subject to SEG license or copyright; see Terms of Use at http://library.seg.org/page/policies/terms
DOI:10.1190/geo2023-0176.1

where $\nabla^2_\xi = (\partial/\partial\xi^1)(\partial/\partial\xi^1) + (\partial/\partial\xi^2)(\partial/\partial\xi^2) + (\partial/\partial\xi^3)(\partial/\partial\xi^3)$ and where we assume the medium velocity is slowly varying (i.e., $(\partial c/\partial\xi^i) \approx 0$ for $i = 1, 2, 3$).

Numerical implementation

We use a FD approach to solve the second-order AWE (equation 8) by approximating the partial differential operators with Taylor-expansion coefficients. The numerical scheme uses approximations of order $O(\Delta\xi^4)$ for spatial derivatives and $O(\Delta\tau^2)$ for temporal derivatives. The fluid advection term in equation 8 is a first-order mixed derivative that presents a challenge in numerical implementation because it requires the spatial derivative of the pressure field at a future time step that is unavailable, when using a second-order approximation centered in time. To overcome this problem, we can use either a first-order approximation backward in time or predict the future time step assuming no source motion (e.g., Van Renterghem and Botteldooren, 2007; Konuk and Shragge, 2020). Although the first approach can still use a fourth-order approximation for the first-order spatial partial differential operator, it reduces the accuracy of the numerical scheme by using a first-order approximation for the first-order temporal partial differential operator backward in time. The second approach allows for maintaining a second-order approximation for all temporal differential operators in the AWE by predicting a future pressure wavefield, assuming a stationary source. Such an assumption is valid because the horizontal mesh deformation is represented by a smooth continuous function with a small contribution to the pressure wavefield (i.e., $v \ll c$) (Konuk and Shragge, 2020). Implementing the second-order AWE permits modeling moving sources using a standard Cartesian-based modeling method with relatively minor modifications. In our numerical implementation, we use Clayton-Enquist absorbing boundary condition (Clayton and Engquist, 1977) for its simplicity and ease of implementation when solving the second-order AWE. Synthetic examples show that the numerical scheme is stable and sufficiently accurate.

Doppler effect

In a constant velocity medium, the source motion causes time-dependent frequency shifts in the data given by

$$f(t) = \frac{c}{c - \mathbf{S}\cdot\mathbf{P}(t)} f_\circ(t), \tag{9}$$

where $f(t)$ is the time-dependent observed frequency, c is the medium wave propagation speed, $\mathbf{S}$ is the source velocity vector, $\mathbf{P}(t)$ is the time-dependent unit vector that points to the receiver or a scatterer point from the source location (Figure 2a), and $f_\circ(t)$ is the time-dependent input frequency.

For heterogeneous media, the raypaths from a source to a scattering point play a role in the amount of frequency shift. To derive an expression for the frequency change due to source motion in heterogeneous media, we follow the formulation of Kolano (1978). We consider a moving source with velocity v and a stationary point in the subsurface (Figure 2b). We assume that the source at time $t = 0$ s is at S_1 and after a time interval Δt it is at S_2. If the source emits two pulses, one at each location, the time delay between emitting these pulses will be Δt. The raypaths the two pulses take to arrive at the same location R are P_1 and P_2, with the associated traveltimes T_1 and T_2, respectively. The time delay between the two pulses at R is

$$\Delta\tau = \Delta t + T_2 - T_1 = \Delta t - \Delta T. \tag{10}$$

Considering a source emitting continuously when moving from S_1 to S_2, and because the total number of emitted cycles matches the total number of observed cycles, we have

$$f_\circ \Delta t = f \Delta\tau, \tag{11}$$

where $f_\circ$ and f are the emitted and observed frequencies, respectively. Thus, the frequency shift is

$$\Delta f = \frac{\Delta T}{\Delta\tau} f_\circ = \frac{\Delta T}{\Delta t - \Delta T} f_\circ, \tag{12}$$

which reduces to

$$\Delta f \approx \frac{\Delta T}{\Delta t} f_\circ, \tag{13}$$

for $(\Delta T/\Delta t) \ll 1$ (i.e., the source velocity is much slower than the wave propagation speed). As Δt approaches zero,

$$\Delta f = \lim_{\Delta t\to 0} \frac{T_2 - T_1}{\Delta t} f_\circ = \lim_{\Delta t\to 0} \frac{-\Delta T}{\Delta t} f_\circ = -\frac{dT}{dt} f_\circ. \tag{14}$$

Equation 14 shows that the Doppler effect in heterogeneous media is related to the material property along the raypath from the source to any point of interest in the subsurface. A more detailed treatment of the Doppler effect in complex media (e.g., anisotropic media) is commonly found in the physics literature concerning radio waves propagating through the ionosphere (e.g., Weekes, 1958; Davies, 1965; Bennett, 1968).

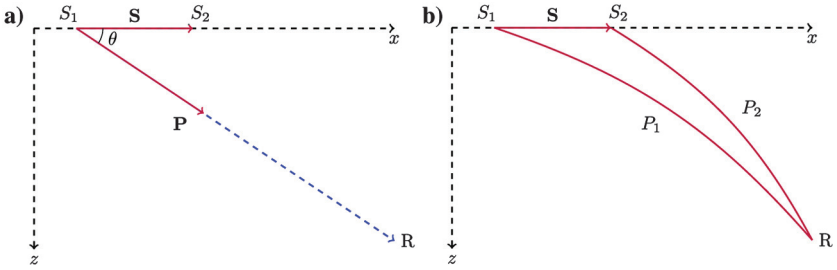

Figure 2. Schematic plot of (a) source motion direction ($\mathbf{S}$) relative to a stationary receiver or a scatterer point location ($\mathbf{R}$) in a constant velocity medium and (b) a source moving from S_1 to S_2 with raypaths from source locations S_1 and S_2 to a point R in the subsurface given by P_1 and P_2, respectively, in a variable velocity medium.

NUMERICAL EXAMPLES

In this section, we present numerical examples to demonstrate the effect of source motion on seismic data in homogeneous media and on ghost reflections using a single-reflector model. We also investigate the impact of medium heterogeneity on the Doppler effect and numerically validate our modeling approach by comparing the observed frequencies from our simulations with those predicted by the Doppler theory. Finally, we examine the effects of source and receiver motion in complex media.

Downloaded 01/12/24 to 138.67.12.184. Redistribution subject to SEG license or copyright; see Terms of Use at http://library.seg.org/page/policies/terms
DOI:10.1190/geo2023-0176.1

Modeling in homogeneous media

In horizontally invariant media, one can set $\gamma = 0$ in equation 6, reducing the mesh deformation to a pure horizontal translation along the source motion direction. A positive (negative) velocity translates the mesh along the positive (negative) ξ^1-axis. To demonstrate the robustness of the developed approach and highlight the consequences of source motion on seismic data, we use an unrealistically fast source velocity of 0.3 km/s in a homogeneous medium. We simulate a 2D acoustic wavefield in a constant velocity medium of 1.5 km/s using a 30 Hz monochromatic wave. The source is located at $x^1 = 2.0$ km (i.e., $\xi^1 = 2.0$ km) at time $t = 0$ s. In the mobile source case, we compute the acoustic wavefield using our approach and interpolate it to the Cartesian coordinate system at every time step. Figure 3a and 3b shows snapshots at $t = 0.68$ s modeled using stationary and mobile sources, respectively. In the stationary source scenario, the wavefield is symmetric and the amplitudes along a wavefront are uniform. In the mobile source scenario, the right-going waves (along the source movement direction) are compressed, whereas the waves traveling in the opposite direction are dilated, according to the Doppler effect. The amount of compression or dilation is a function of the source velocity, the acoustic wave propagation speed in the medium, the source motion direction, the propagation direction, and the input frequency.

Figure 4a and 4b shows shot gathers acquired using stationary and mobile sources, respectively, recorded using stationary receivers placed 25 m below the source. For the stationary source case (Figure 4a), the direct arrivals are symmetric around the source location. For the mobile source case (Figure 4b), the apices of the direct arrivals are shifted because of the source motion and the lateral shift increases with time. Traces recorded to the left of the source are shifted to a lower frequency, whereas the traces recorded to the right of the source are shifted to a higher frequency. Figure 5b and 5c shows two traces for stationary receivers at $x^1 = 1.75$ km and $x^1 = 2.75$ km, respectively, placed at the same depth level as the source, computed numerically and analytically (we derive the analytical solution in Appendix A). Although the input source (Figure 5a) is a 30 Hz monochromatic wave (Figure 6a), the trace to the left of the source is dilated compared to that to the right of the source. The corresponding amplitude spectra (Figure 6b and 6c) indicate that the observed frequency at the left receiver is 25 Hz, whereas the observed frequency at the right receiver is 37.5 Hz. Our numerical results match the theoretical observed frequencies using the Doppler (1842) formula and closely match the analytical results, thereby demonstrating the accuracy and stability of the developed modeling approach outlined previously.

Modeling in a single-reflector model

To demonstrate the effects of source motion on ghost reflections, we simulate stationary and mobile source data with ghost reflections in a single-reflector model (Figure 7) using a source function with a linear sweep between 25 Hz and 45 Hz placed at $x^3 = 0.05$ km (i.e., $\xi^1 = 0.05$ km) at time $t = 0$ s and stationary receivers placed 25 m below the source. To model mobile source data, we use a fast source velocity of 0.3 km/s. The ghost reflections in the stationary source data (Figure 8a) are symmetric around the

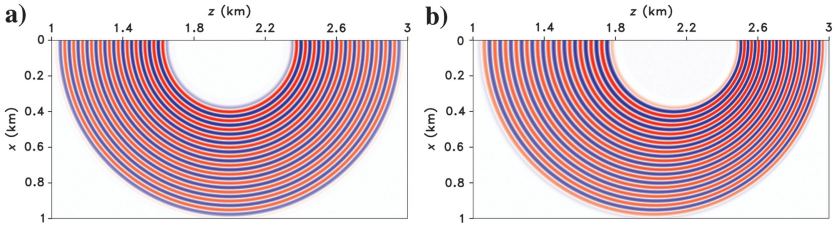

Figure 3. Wavefield snapshot in a homogeneous medium using (a) stationary and (b) mobile sources.

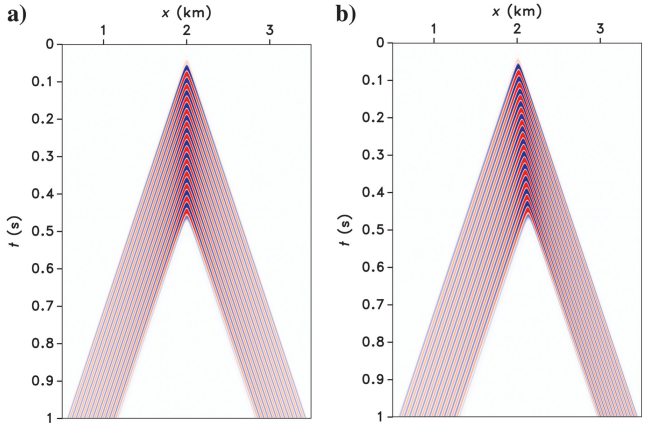

Figure 4. Shot gathers acquired in a homogeneous medium using (a) stationary and (b) mobile sources.

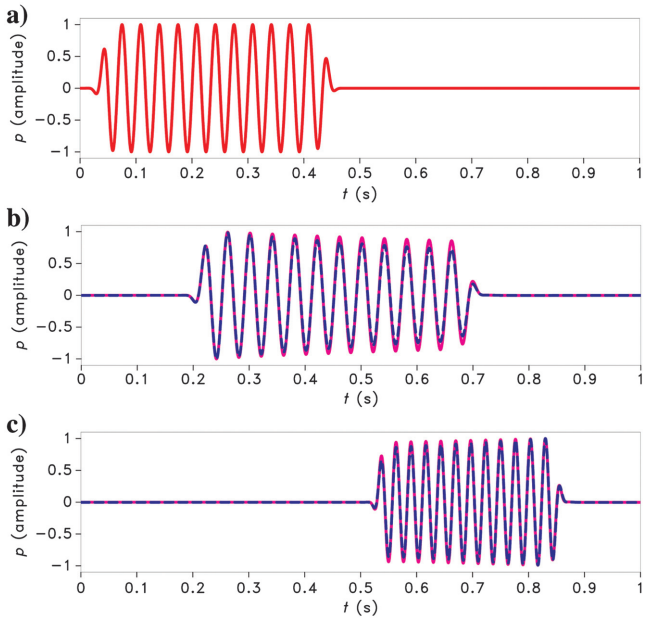

Figure 5. Pressure amplitude of (a) 30 Hz monochromatic wave (source function) and seismic data measured by receivers located (b) behind ($x^1 = 1.75$ km) and (c) ahead ($x^1 = 2.75$ km) of the source. The dashed line is the analytical solution, which overlay the numerical solution shown in solid line.

Downloaded 01/12/24 to 138.67.12.184. Redistribution subject to SEG license or copyright; see Terms of Use at http://library.seg.org/page/policies/terms
DOI:10.1190/geo2023-0176.1

source location, whereas they are slanted in time in the mobile source data (Figure 8b). However, the frequency-wavenumber spectra of the stationary source data (Figure 9a) and the mobile source data (Figure 9b) show that the constructive and destructive interference caused by ghost reflections are unaffected by the source motion because such interference in the Fourier domain are determined solely by the time delay between the primary signal and its ghost, which remains unchanged between stationary and mobile source modeling.

Modeling in a velocity gradient medium

To understand the consequences of velocity variation on the Doppler effect, we simulate mobile source data in homogeneous (Figure 10a) and constant vertical velocity gradient (Figure 10b) models using an unrealistically fast source velocity of 0.3 km/s. For the homogeneous model, the medium velocity is 2.0 km/s. For the constant vertical velocity gradient model, the medium velocity is given by the function $c(\xi^3) = 1.0 + 0.5\xi^3$m/s, with a maximum depth of 4.0 km. We simulate these data types using a 40 Hz monochromatic wave placed at $[x^1, x^3] = [2.0, 2.0]$km (i.e., $[\xi^1, \xi^3] = [2.0, 2.0]$km) at time $t = 0$ s and stationary vertical receivers placed at $x^1 = 3.0$ km. Figure 11 shows traces recorded by receivers placed at $x^3 = 1.25$ km and $x^3 = 2.75$ km, their amplitude spectra, and the theoretical observed frequencies as a function of depth for the homogeneous velocity model. Because the velocity model is constant, and because the two receivers are symmetric around the source depth location, the two traces have the same observed frequency. Furthermore, the theoretical observed frequencies as a function of depth, computed using equation 12, show that the observed frequency profile also is symmetric around the source locations, i.e., the Doppler effect depends on the angle between the source and receiver. Figure 12 shows traces recorded by receivers placed at $x^3 = 1.25$ km and $x^3 = 2.75$ km, their amplitude spectra, and the theoretical observed frequencies as a function of depth for the constant vertical velocity gradient model. In this case, the source is moving in a constant layer, but the two traces have different observed frequencies even though the two receivers are symmetric

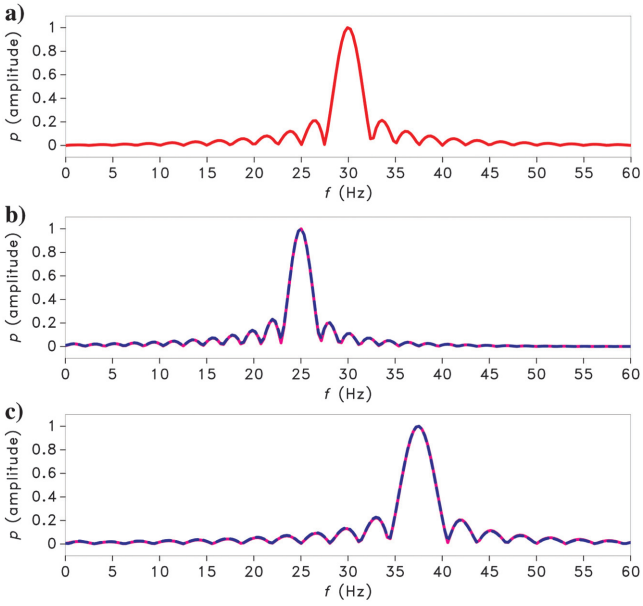

Figure 6. (a–c) Amplitude spectra of traces shown in Figure 5a–5c, respectively. The dashed line is the analytical solution, which overlay the numerical solution shown in solid line.

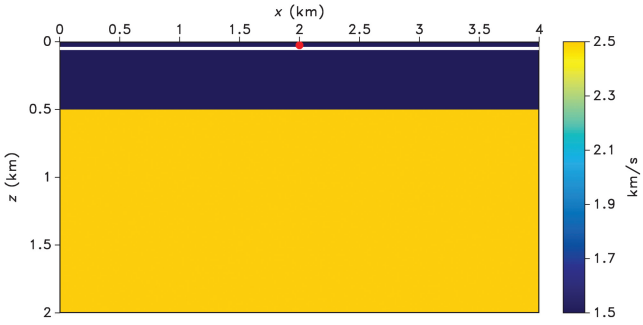

Figure 7. Single-reflector velocity model with the source position at time $t = 0$ s (red) and stationary receiver locations (white).

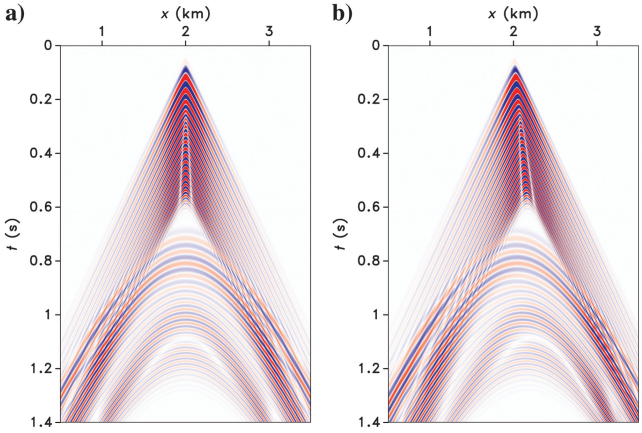

Figure 8. Shot gathers acquired in a single-reflector model using (a) stationary and (b) mobile sources with ghost reflections.

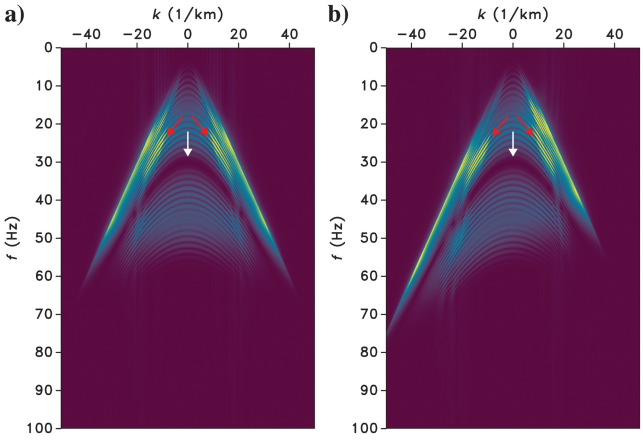

Figure 9. Frequency-wavenumber spectra of shot gathers shown in (a) Figure 8a and (b) Figure 8b. The red and white arrows indicate constructive and destructive interference, respectively.

Downloaded 01/12/24 to 138.67.12.184. Redistribution subject to SEG license or copyright; see Terms of Use at http://library.seg.org/page/policies/terms
DOI:10.1190/geo2023-0176.1

around the source depth position. The theoretical observed frequency profile is asymmetric, highlighting the significance of traveltime changes due to velocity variations in the Doppler effect.

Modeling in heterogeneous media

To investigate the impact of source motion on seismic data acquisition in heterogeneous media, we simulate the acoustic wavefield using the Marmousi II model (Martin et al., 2002). We use a source placed at $[\xi^1, \xi^3] = [8.5, 0.0125]$km and 3601 receivers positioned at $\xi^3 = x^3 = 0.45$ km, with a 2.5 m uniform spacing. We use a source velocity of 5 m/s, which exceeds the typical acquisition source speed of 2–3 m/s, to emphasize the discrepancies between stationary and mobile source acquisition. Figure 13a shows the velocity model with the source position at time $t = 0$ s and stationary receiver locations. The source function is a linear sweep from 15 Hz to 43 Hz. Figure 14a and 14b shows the shot gathers acquired using stationary and mobile sources, respectively. Although the shot gathers may appear similar at first glance, the difference between the two demonstrates that source motion has a discernible effect on the seismic data in amplitude and phase (Figure 14c). Figure 15 shows traces recorded by a receiver located at $x^1 = 4.5$ km for the stationary (black) and mobile (red) source acquisition, demonstrating the amplitude and phase discrepancies between the two acquisitions. It is important to note that, whereas the discrepancies may be insignificant for low frequencies and slow source velocities, the motion of the source can introduce artifacts if not properly addressed in the processing workflow at high frequencies or when source velocities are high (Guitton et al., 2021).

Guitton et al. (2021) and Almuteri et al. (2022) show that ignoring source motion effects in RTM introduces phase shift and mispositioning of imaged structures. Because of the long sweep duration and continuous source motion, the wavefield is altered due to the source changing its position while emitting energy (Hampson and Jakubowicz, 1995), i.e., the earth is illuminated differently when using a moving source than when using a stationary source. To show the effects of source motion on RTM results, we use a Marmousi II submodel to simulate two data sets with and without moving sources. We use 93 sources placed at $\xi^3 = 0.0125$ km with a 25 m source-initiation interval spacing, and we use 199 receivers placed at $\xi^3 = 0.375$ km with a 12.5 m receiver spacing. We model data for a 2.5 s record length at a 0.5 ms temporal sampling interval. For the moving source acquisition, we use a high source

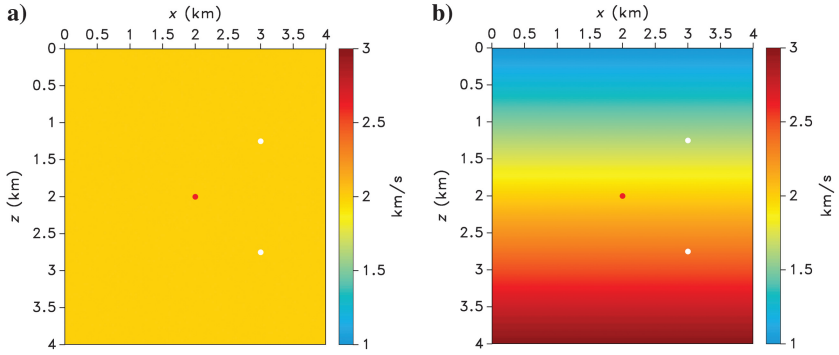

Figure 10. (a) Homogeneous and (b) constant vertical velocity gradient models with the source position at time $t = 0$ s (red) and stationary receiver locations (white).

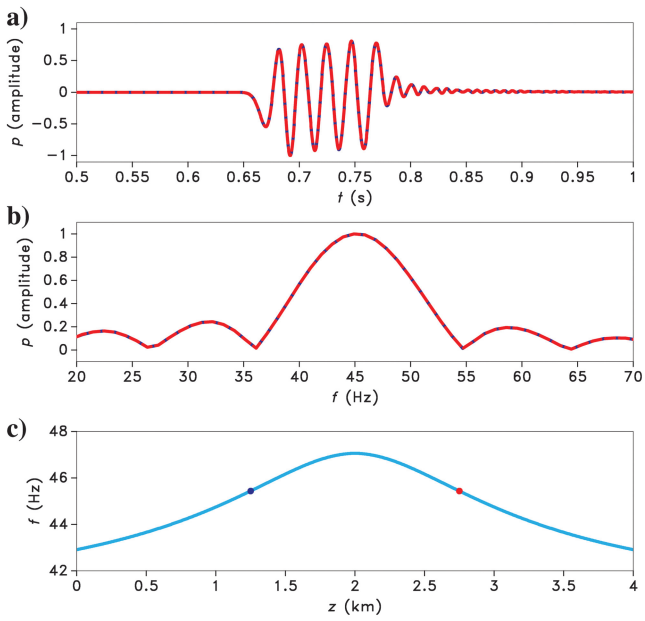

Figure 11. Mobile source in a homogeneous medium. (a) Seismic data measured by receivers located at $x^3 = 1.25$ km (blue) and $x^3 = 2.75$ km (red). (b) Corresponding amplitude spectra of traces shown in (a). (c) Theoretical observed frequencies as a function of depth.

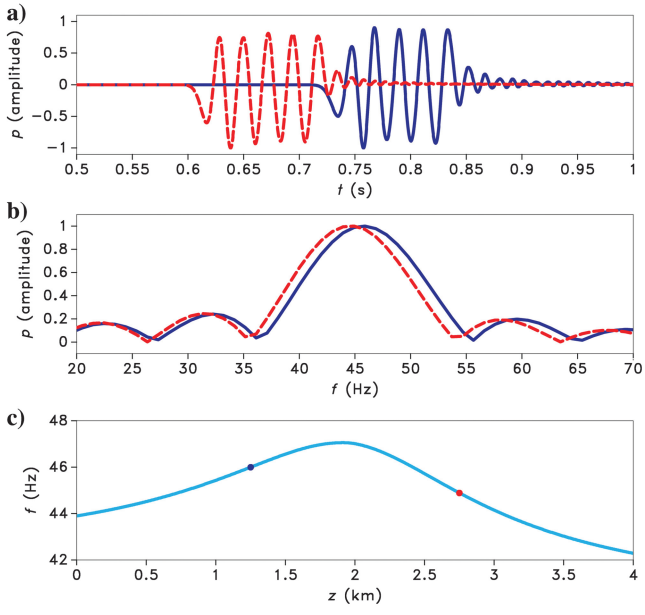

Figure 12. Mobile source in a velocity gradient medium. (a) Seismic data measured by receivers located at $x^3 = 1.25$ km (blue) and $x^3 = 2.75$ km (red). (b) Corresponding amplitude spectra of traces shown in (a). (c) Theoretical observed frequencies as a function of depth.

Downloaded 01/12/24 to 138.67.12.184. Redistribution subject to SEG license or copyright; see Terms of Use at http://library.seg.org/page/policies/terms
DOI:10.1190/geo2023-0176.1

velocity of 10 m/s to highlight the significance of source motion on seismic imaging. The source function is a linear sweep from 20 Hz to 40 Hz. The RTM image of the stationary acquisition and imaging (Figure 16a) and the mobile acquisition and stationary imaging (Figure 16b) look similar; however, the difference between the two (Figure 16c) shows a phase change and mispositioning of imaged structures, demonstrating the importance of accounting for source motion effects in processing or imaging.

To investigate the impact of receiver motion on seismic data, we simulate the acoustic wavefield using a Ricker wavelet with a 40 Hz dominant frequency to mimic a marine impulsive source. We use a source placed at $[\xi^1, \xi^3] = [3.5, 0.0125]$km and receivers positioned at the same depth as the source. We use 3601 receivers with a 2.5 m uniform spacing with the first and last receivers at the initial time placed at $\xi^1 = 4.0$ km and $\xi^1 = 13.0$ km, respectively, being towed at 5 m/s velocity. Figure 13b shows the velocity model with the stationary source position and receivers locations at time $t = 0$ s. Figure 17a and 17b shows the shot gathers acquired using stationary and mobile receivers, respectively. Similar to the mobile source example, the receiver motion changes amplitude and phase compared to the stationary receiver acquisition (Figure 17c). Figure 18 shows traces recorded by a receiver located at $x^1 = 9$ km at time $t = 0$ s (trace number 2000) for the stationary (black) and mobile (red) receiver acquisition, which clearly show the discrepancies between the two acquisitions. The receiver motion does not alter the seismic wavefield, as opposed to a mobile source experiment, but rather samples the wavefield along a slanted trajectory in time and space, which can normally be ignored as discussed by Hampson and Jakubowicz (1995). However, the source motion in marine vibrator acquisition cannot be ignored because of the long duration of the source and its continuous motion.

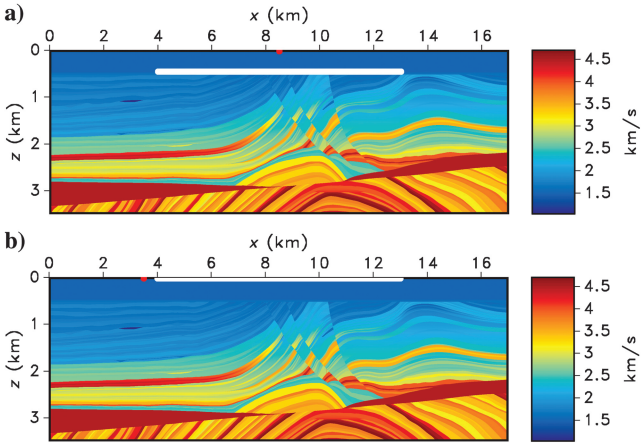

Figure 13. Marmousi II velocity model with the source position (red) and receiver locations (white) at time $t = 0$ s for (a) moving source and stationary receivers (ocean bottom) acquisition and (b) stationary source and moving receivers (streamer) acquisition. Figure is not displayed with the true aspect ratio.

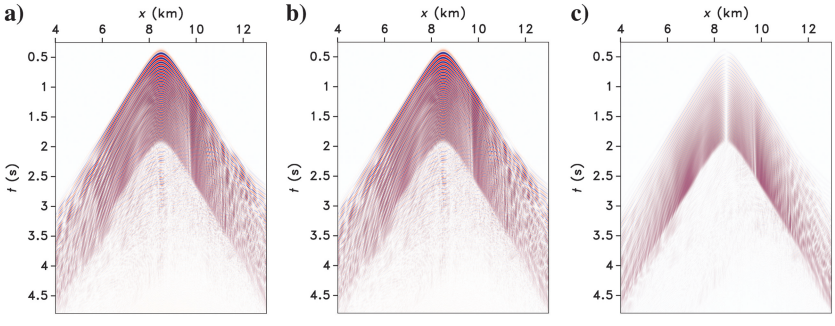

Figure 14. Shot gathers acquired using the Marmousi II model for (a) a stationary source and (b) mobile source. (c) Difference between (a) and (b).

DISCUSSION

Source motion introduces frequency shifts that are proportional to the source velocity, acoustic wave velocity in the medium, propagation direction, and input frequency. The frequency shifts in the modeled seismic data are more pronounced at high frequencies, even with a slow source velocity. More importantly, medium heterogeneity between the source and receiver, or any point in the subsurface, plays a role in the Doppler shift. Neglecting frequency shifts and the time-dependent source-receiver offset in seismic data processing and imaging introduces artifacts in the processed data and ensuing imaging and/or inversion workflows. Although source motion causes noticeable frequency shifts in data, a change in source position when emitting is expected to have a more significant impact on seismic processing and imaging.

Under quiescent sea-surface conditions, ghost reflections interfere with the primary signal in mobile and stationary acquisition in a similar manner. However, in stationary acquisition, source-side ghost reflections are described by an effective static sea surface (Blacquière and Sertlek, 2019), i.e., they occur instantaneously. However, for moving and long-emitting sources, source-side ghost reflections are explained using a dynamic sea surface model. Understanding the effects of ghost reflections on marine vibrator data under realistic time-varying sea surface conditions is critical for developing robust seismic deghosting solutions for this type of acquisition. Therefore, future work involves incorporating a dynamic sea surface to mimic more realistic marine vibrator acquisition scenarios.

Our numerical results show that solving the second-order AWE using a FD approach with Taylor-expansion coefficients is accurate and stable. Adopting such an approach enables obtaining reliable subsurface images and reduces interpretation uncertainties. Although time-dependent meshes require repeated and expensive interpolation of the physical properties of the subsurface, the proposed work mitigates the need for such interpolations by using a judicious coordinate transformation to confine the mesh deformation to the homogeneous water layer. In addition, the proposed methodology helps improve marine acquisition design and processing by providing reliable and robust tools for numerical experimentation. The developed approach also can be used in RTM to image marine vibrator data because of its intrinsic ability to account for source motion effects when computing required source and receiver wavefields, which we leave for future work.

Downloaded 01/12/24 to 138.67.12.184. Redistribution subject to SEG license or copyright; see Terms of Use at http://library.seg.org/page/policies/terms
DOI:10.1190/geo2023-0176.1

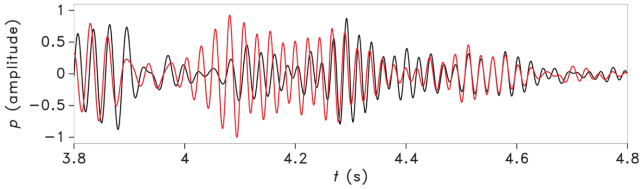

Figure 15. Seismic data measured by a receiver located at $x^1 = 4.5$ km for a stationary source (black) and mobile source (red).

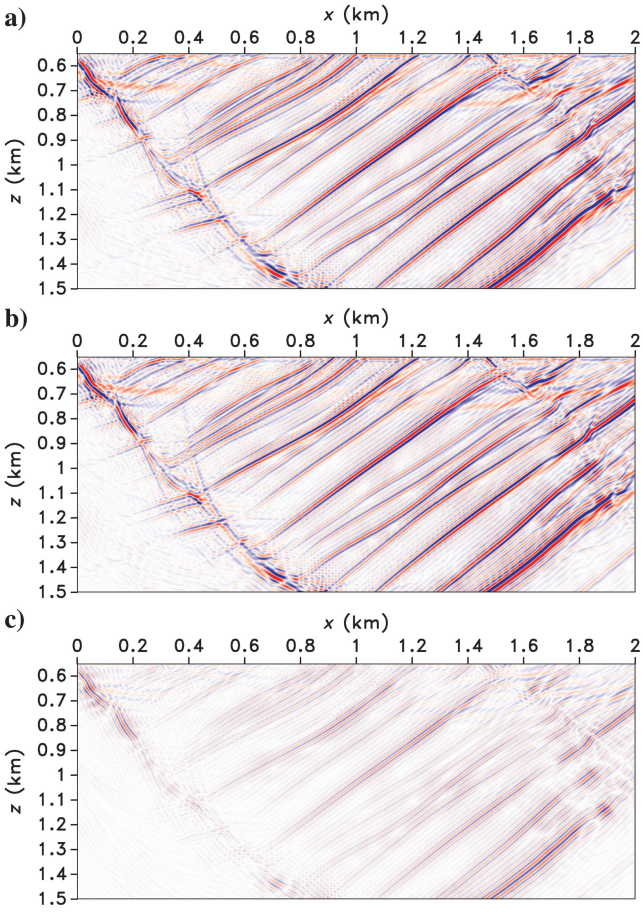

Figure 16. The RTM image for (a) stationary acquisition and imaging and (b) mobile acquisition and stationary imaging. (c) Difference between (a) and (b).

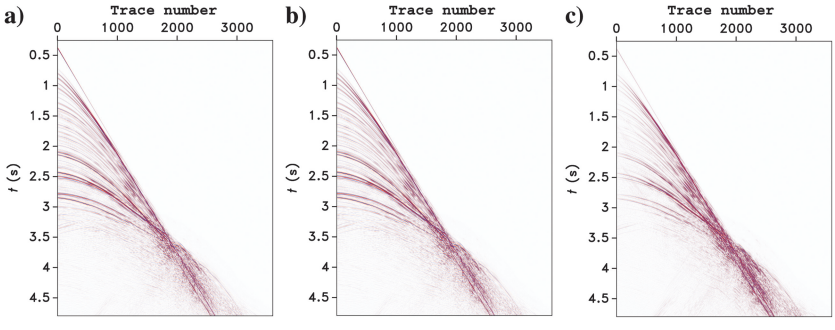

Figure 17. Shot gathers acquired using the Marmousi II model for (a) stationary and (b) mobile receivers. (c) Difference between (a) and (b).

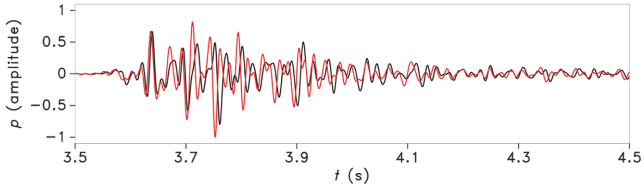

Figure 18. Seismic data measured by a receiver located at $x^1 = 9$ km at time $t = 0$ s (trace number 2000) for a stationary receiver (black) and mobile receiver (red).

CONCLUSION

We present a finite-difference approach for solving the acoustic wave equation to simulate marine vibrator data. The developed method uses a geometric coordinate transformation to compute the full acoustic wavefield on a uniformly spaced and time-invariant mesh grid. Although our implementation assumes constant source motion, incorporating a variable velocity moving source into this framework is straightforward. The proposed numerical approach can accurately and stably model seismic wavefields, even at unrealistically high velocities of the moving source. Furthermore, this work is not only limited to modeling marine vibrators but also can be used to model towed-streamer data using impulsive sources.

ACKNOWLEDGMENTS

The first author would like to thank Saudi Aramco for graduate study sponsorship. We thank the sponsors of the Center for Wave Phenomena at Colorado School of Mines for the support of this research. We also thank A. Guitton (TotalEnergies) and T. Konuk (Nvidia) for many useful discussions. Reproducible numerical examples were generated using the Madagascar open-source software package freely available from http://www.ahay.org. Analytic coordinate system geometry results were verified using the Mathematica software package from https://www.wolfram.com/mathematica/.

DATA AND MATERIALS AVAILABILITY

Data associated with this research are available and can be obtained by contacting the corresponding author.

APPENDIX A

ANALYTICAL SOLUTION TO THE AWE FOR A MOVING SOURCE

The Green's function for the AWE for a moving source is given by (Jackson, 1999; Ahrens and Spors, 2011)

$$G(\mathbf{x}, t; \mathbf{x}_s(t_s), t_s) = \frac{\delta\left(t - t_s - \frac{|\mathbf{x}-\mathbf{x}_s(t_s)|}{c}\right)}{|\mathbf{x}-\mathbf{x}_s(t_s)|}, \tag{A-1}$$

where $\mathbf{x} = [x, y, z]$ is the 3D space variable, t is the time variable, t_s is the source emission time, $\mathbf{x}_s(t_s) = [x_s(t_s), y_s(t_s), z_s(t_s)]$ is the source position as a function of emission time, and c is the constant medium velocity. Thus, the wavefield $P(\mathbf{x}, t)$ for an arbitrary source function $f(t_s)$ is

Downloaded 01/12/24 to 138.67.12.184. Redistribution subject to SEG license or copyright; see Terms of Use at http://library.seg.org/page/policies/terms
DOI:10.1190/geo2023-0176.1

$$P(\mathbf{x},t) = \int_{-\infty}^{\infty} f(t_s) G(\mathbf{x},t;\mathbf{x}_s(t_s),t_s)\mathrm{d}t_s$$
$$= \int_{-\infty}^{\infty} f(t_s) \frac{\delta\left(t - t_s - \frac{|\mathbf{x}-\mathbf{x}_s(t_s)|}{c}\right)}{|\mathbf{x}-\mathbf{x}_s(t_s)|}\mathrm{d}t_s$$
$$= \int_{-\infty}^{\infty} f(t_s) \frac{\delta(t-t_s-\tau)}{c\tau}\mathrm{d}t_s, \quad \text{(A-2)}$$

where $\tau(\mathbf{x},t_s) = (|\mathbf{x}-\mathbf{x}_s(t_s)|/c)$. To evaluate equation A-2, we introduce a new variable $u = t_s + \tau(\mathbf{x},t_s)$, resulting in

$$P(\mathbf{x},t) = \int_{-\infty}^{\infty} f(u-\tau)\frac{\delta(t-u)}{c\tau}\mathrm{d}u \quad = \frac{f(t-\tau)}{c\tau}, \quad \text{(A-3)}$$

where we use the sifting property of the delta function. Now, considering a source moving along a straight path with a velocity $\mathbf{v} = [v_x, v_y, v_z]$, we can express the source position as a function of emission time as a Galilean transformation:

$$\mathbf{x}_s(t_s) = \mathbf{x}_s(0) + \mathbf{v}t_s, \quad \text{(A-4)}$$

where $\mathbf{x}_s(0)$ is the source position at time zero. We can rewrite equation A-4 in terms of an arbitrary recording time t by introducing a new variable R such that $t_s = t - (R/c)$, where $R = |\mathbf{R}|$ and $\mathbf{R} = \mathbf{x} - \mathbf{x}_s(t_s)$, as

$$\mathbf{x}_s(t) = \mathbf{x}_s(0) + \mathbf{v}\left(t - \frac{R}{c}\right). \quad \text{(A-5)}$$

Therefore, we can find the source position for any emitted signal (when emitted) as a function of recording time t and receiver position $\mathbf{R}$, needed to evaluate equation A-3. To derive the analytical solution to the AWE for a moving source, we follow the formulation of Morse and Ingard (1986) to find R. Because $R = |\mathbf{x} - \mathbf{x}_s(t_s)|$, we have

$$\begin{aligned}
R^2 &= (x-x_s(t_s))^2 + (y-y_s(t_s))^2 + (z-z_s(t_s))^2 \\
&= (x-x_s(0)-v_x t_s)^2 + (y-y_s(0)-v_y t_s)^2 + (z-z_s(0)-v_z t_s)^2 \\
&= \left(x-x_s(0)-v_x\left(t-\frac{R}{c}\right)\right)^2 + \left(y-y_s(0)-v_y\left(t-\frac{R}{c}\right)\right)^2 \\
&\quad + \left(z-z_s(0)-v_z\left(t-\frac{R}{c}\right)\right)^2 \\
&= (x-x_s(0)-v_x t + M_x R)^2 + (y-y_s(0)-v_y t + M_y R)^2 \\
&\quad + (z-z_s(0)-v_z t + M_z R)^2 \\
&= (\tilde{x}+M_x R)^2 + (\tilde{y}+M_y R)^2 + (\tilde{z}+M_z R)^2, \quad \text{(A-6)}
\end{aligned}$$

where $\tilde{x} = x - x_s(0) - v_x t$, $\tilde{y} = y - y_s(0) - v_y t$, $\tilde{z} = z - z_s(0) - v_z t$, and $\mathbf{M} = [M_x, M_y, M_z] = [(v_x/c), (v_y/c), (v_z/c)]$. We solve for R in equation A-6, using the quadratic formula, to obtain

$$R = \frac{\mathbf{M}\cdot\tilde{\mathbf{x}} \pm \sqrt{(1-\mathbf{M}\cdot\mathbf{M})(\tilde{\mathbf{x}}\cdot\tilde{\mathbf{x}}) + (\mathbf{M}\cdot\tilde{\mathbf{x}})^2}}{1-\mathbf{M}\cdot\mathbf{M}}, \quad \text{(A-7)}$$

where $\tilde{\mathbf{x}} = [\tilde{x}, \tilde{y}, \tilde{z}]$. Assuming $\mathbf{M}\cdot\mathbf{M} < 1$, i.e., the source velocity is slower than the wave propagation speed, R is strictly positive only for (Morse and Ingard, 1986)

$$R = \frac{\mathbf{M}\cdot\tilde{\mathbf{x}} + \sqrt{(1-\mathbf{M}\cdot\mathbf{M})(\tilde{\mathbf{x}}\cdot\tilde{\mathbf{x}}) + (\mathbf{M}\cdot\tilde{\mathbf{x}})^2}}{1-\mathbf{M}\cdot\mathbf{M}}. \quad \text{(A-8)}$$

As a result, the analytical solution to the AWE for a moving source is

$$P(\mathbf{x},t) = \frac{f\left(t-\frac{R}{c}\right)}{R}, \quad \text{(A-9)}$$

where R is given in equation A-8. We use equation A-9 to compute the analytical solution of the AWE for a moving source in a homogeneous medium and validate our numerical approach.

REFERENCES

Ahrens, J., and S. Spors, 2011, Wave field synthesis of moving virtual sound sources with complex radiation properties: The Journal of the Acoustical Society of America, **130**, 2807–2816, doi: 10.1121/1.3640850.

Almuteri, K., P. Sava, and J. Shragge, 2022, Reverse-time migration of mobile marine vibrator data: Second International Meeting for Applied Geoscience & Energy, Expanded Abstracts, 2694–2698, doi: 10.1190/image2022-3751755.1.

Amundsen, L., F. Andersson, D.-J. van Manen, J. O. A. Robertsson, and K. Eggenberger, 2018, Multisource encoding and decoding using the signal apparition technique: Geophysics, **83**, no. 1, V49–V59, doi: 10.1190/geo2017-0206.1.

Bennett, J. A., 1968, The ray theory of Doppler frequency shifts: Australian Journal of Physics, **21**, 259–272, doi: 10.1071/PH680259.

Blacquière, G., and H. O. Sertlek, 2019, Modeling and assessing the effects of the sea surface, from being flat to being rough and dynamic: Geophysics, **84**, no. 2, T13–T27, doi: 10.1190/geo2018-0294.1.

Clayton, R., and B. Engquist, 1977, Absorbing boundary conditions for acoustic and elastic wave equations: Bulletin of the Seismological Society of America, **67**, 1529–1540, doi: 10.1785/BSSA0670061529.

Davies, K., 1965, Ionospheric radio propagation: U.S. Department of Commerce, National Bureau of Standards, 80.

Dellinger, J., and E. Díaz, 2020, Efficient modelling of extended-duration moving seismic sources: 82nd Annual International Conference and Exhibition, EAGE, Extended Abstracts, doi: 10.3997/2214-4609.202010838.

Dellinger, J., A. Ross, D. Meaux, A. Brenders, G. Gesoff, J. Etgen, J. Naranjo, G. Openshaw, and M. Harper, 2016, Wolfspar®, an "FWI-friendly" ultra-low-frequency marine seismic source: 86th Annual International Meeting, SEG, Expanded Abstracts, 4891–4895, doi: 10.1190/segam2016-13762702.1.

Doppler, C., 1842, Ueber das farbige licht der Doppelsterne und einiger anderer Gestirne des Himmels: Versuch einer das Bradley'sche Aberrations-Theorem als integrirenden Theil in sich schliessenden allgemeineren Theorie: K. Böhm Gesellschaft der Wissenschaften, 465–482.

Dragoset, W. H., 1988, Marine vibrators and the Doppler effect: Geophysics, **53**, 1388–1398, doi: 10.1190/1.1442418.

Duquet, B., A. Guitton, S. Secker, A. Feltham, and J.-P. Mascomere, 2021, Impact of non-impulsive moving source correction for structural and 4D imaging: First International Meeting for Applied Geoscience & Energy, Expanded Abstracts, 31–35, doi: 10.1190/segam2021-3594448.1.

Egan, M., K. G. El-Kasseh, and N. Moldoveanu, 2007, Full deghosting of OBC data with over/under source acquisition: 77th Annual International Meeting, SEG, Expanded Abstracts, 31–35, doi: 10.1190/1.2792376.

Guitton, A., B. Duquet, S. Secker, J. P. Mascomere, and A. Feltham, 2021, A deconvolution-interpolation approach with sparse inversion to mitigate the Doppler effect in marine vibrators data: First International Meeting for Applied Geoscience & Energy, Expanded Abstracts, 2555–2559, doi: 10.1190/segam2021-3593897.1.

Halliday, D. F., and I. Moore, 2018, A comparison of random and periodic marine simultaneous-source encoding: The Leading Edge, **37**, 471a1–471a11, doi: 10.1190/tle37060471a1.1.

Hampson, G., and H. Jakubowicz, 1995, The effects of source and receiver motion on seismic data: Geophysical Prospecting, **43**, 221–244, doi: 10.1111/j.1365-2478.1995.tb00133.x.

Jackson, J. D., 1999, Classical electrodynamics: John Wiley & Sons.

JafarGandomi, A., and S. Grion, 2021, Modelling of marine vibrator data: 83rd Annual International Conference and Exhibition, EAGE, Extended Abstracts, doi: 10.3997/2214-4609.202113202.

Kolano, R. A., 1978, Doppler shift in layered media: Master's thesis, Pennsylvania State University.

Konuk, T., and J. Shragge, 2020, Modeling full-wavefield time-varying sea-surface effects on seismic data: A mimetic finite-difference approach: Geophysics, **85**, no. 2, T45–T55, doi: 10.1190/geo2019-0181.1.
Kurzmann, A., A. Przebindowska, D. Köhn, and T. Bohlen, 2013, Acoustic full waveform tomography in the presence of attenuation: A sensitivity analysis: Geophysical Journal International, **195**, 985–1000, doi: 10.1093/gji/ggt305.
Landrø, M., 2008, The effect of noise generated by previous shots on seismic reflection data: Geophysics, **73**, no. 3, Q9–Q17, doi: 10.1190/1.2894453.
Laws, R., D. Halliday, J.-F. Hopperstad, D. Gerez, M. Supawala, A. Özbek, T. Murray, and E. Kragh, 2019, Marine vibrators: The new phase of seismic exploration: Geophysical Prospecting, **67**, 1443–1471, doi: 10.1111/1365-2478.12708.
Martin, G. S., K. J. Marfurt, and S. Larsen, 2002, Marmousi-2: An updated model for the investigation of AVO in structurally complex areas: 72nd Annual International Meeting, SEG, Expanded Abstracts, 1979–1982, doi: 10.1190/1.1817083.
Morse, P. M., and K. U. Ingard, 1986, Theoretical acoustics: Princeton University Press.
Mueller, M. B., D. F. Halliday, D.-J. van Manen, and J. O. Robertsson, 2015, The benefit of encoded source sequences for simultaneous source separation: Geophysics, **80**, no. 5, V133–V143, doi: 10.1190/geo2015-0015.1.
Pawelec, I., M. Wakin, and P. Sava, 2022, Multichannel compressive sensing for seismic data reconstruction using joint sparsity: Second International Meeting for Applied Geoscience & Energy, Expanded Abstracts, 2636–2640, doi: 10.1190/image2022-3751512.1.
Robertsson, J. O., I. Moore, M. Vassallo, K. Özdemir, D.-J. van Manen, and A. Özbek, 2008, On the use of multicomponent streamer recordings for reconstruction of pressure wavefields in the crossline direction: Geophysics, **73**, no. 5, A45–A49, doi: 10.1190/1.2953338.
Robertsson, J. O. A., L. Amundsen, and Å. S. Pedersen, 2016, Signal apparition for simultaneous source wavefield separation: Geophysical Journal International, **206**, 1301–1305, doi: 10.1093/gji/ggw210.
Schultz, P. S., A. W. Pieprzak, G. R. Johnson, and L. Walker, 1989, Simple theory for correction of marine vibroseis phase dispersion: 59th Annual International Meeting, SEG, Expanded Abstracts, 660–662, doi: 10.1190/1.1889560.
Shragge, J., 2014, Solving the 3D acoustic wave equation on generalized structured meshes: A finite-difference time-domain approach: Geophysics, **79**, no. 6, T363–T378, doi: 10.1190/geo2014-0172.1.
Shragge, J., and B. Tapley, 2017, Solving the tensorial 3D acoustic wave equation: A mimetic finite-difference time-domain approach: Geophysics, **82**, no. 4, T183–T196, doi: 10.1190/geo2016-0691.1.
Smith, J. G., and M. R. Jenkerson, 1998, Acquiring and processing marine vibrator data in the transition zone: 68th Annual International Meeting, SEG, Expanded Abstracts, 136–139, doi: 10.1190/1.1820159.
Teyssandier, B., and J. J. Sallas, 2019, The shape of things to come — Development and testing of a new marine vibrator source: The Leading Edge, **38**, 680–690, doi: 10.1190/tle38090680.1.
Van Renterghem, T., and D. Botteldooren, 2007, Prediction-step staggered-in-time FDTD: An efficient numerical scheme to solve the linearised equations of fluid dynamics in outdoor sound propagation: Applied Acoustics, **68**, 201–216, doi: 10.1016/j.apacoust.2005.10.003.
Vassallo, M., A. Özbek, K. Özdemir, and K. Eggenberger, 2010, Crossline wavefield reconstruction from multicomponent streamer data: Part 1 — Multichannel interpolation by matching pursuit (MIMAP) using pressure and its crossline gradient: Geophysics, **75**, no. 6, WB53–WB67, doi: 10.1190/1.3496958.
Weekes, K., 1958, On the interpretation of the Doppler effect from senders in an artificial satellite: Journal of Atmospheric and Terrestrial Physics, **12**, 335–338, doi: 10.1016/0021-9169(58)90064-3.
Zhang, Z., Z. Wu, Z. Wei, J. Mei, R. Huang, and P. Wang, 2023, Enhancing salt model resolution and subsalt imaging with elastic FWI: The Leading Edge, **42**, 207–215, doi: 10.1190/tle42030207.1.
Zhou, W., R. Brossier, S. Operto, J. Virieux, and P. Yang, 2018, Velocity model building by waveform inversion of early arrivals and reflections: A 2D case study with gas-cloud effects: Geophysics, **83**, no. 2, R141–R157, doi: 10.1190/geo2017-0282.1.

Biographies and photographs of the authors are not available.

Downloaded 01/12/24 to 138.67.12.184. Redistribution subject to SEG license or copyright; see Terms of Use at http://library.seg.org/page/policies/terms
DOI:10.1190/geo2023-0176.1